Analysis of ultra-short pulse shaping with programmable amplitude and phase masks

Shanhong You (游善红)[1*], Weidong Shao (邵卫东)[1], Wenfeng Cai (蔡文锋)[1],

Honglong Cao (曹洪龙)[1], and M. Kavehrad[2]

[1]*Institute of Electronic Information, Soochow University, Suzhou 215006, China*

[2]*Department of Electrical Engineering, Pennsylvania State University 111 Electrical Engineering East,*

University Park, PA 16802, USA

*Corresponding author: shyou@suda.edu.cn

Received September 21, 2010; accepted November 2, 2010; posted online February 21, 2011

Specified ultra-short pulse waveforms could be synthesized with high-resolution zero-dispersion pulse shaping system. The system and parameters are analyzed and discussed. The pulse shaping system with optimized parameters could resolve the frequency components of ultra-broad bandwidth pulse and prevent the spatial shaping of individual frequency components. The specified waveforms, Meyer wavelet and square root raised cosine pulses, are generated with programmable amplitude and phase masks.

OCIS codes: 320.5540, 300.6530, 060.2605.

doi: 10.3788/COL201109.033201.

Ultra-short pulsed lasers have recently been considered for optical wireless communications and ultra-wideband communications. Different pulse shapes have been examined with respect to communication system performance, and it has been concluded that waveforms of the Meyer wavelet family best suit multi-rate optical wireless communications[1−3].

The key point for generating arbitrarily shaped optical waveforms with pulse shaping techniques[4−17] is that waveform synthesis is achieved by parallel modulation in the frequency domain. The pulse shaping process depends on the spatial separation of different frequency components at the mask, where selective spectral manipulations take place for different absorption and delay properties of the separate mask regions. However, each individual frequency component has a finite spatial extent at the mask, thus the different spatial regions of a single component may encounter different optical properties. This results in the spatial shaping of individual frequency components.

In this letter, we show that an optimized high-resolution zero-dispersion pulse shaping system can be used to synthesize ultra-short pulse waveforms to specifications. We analyze zero-dispersion pulse shaping system and discuss the parameters. The optimized pulse shaping system can resolve the frequency components of a given repetition rate mode-locked femtosecond laser in the mask plane and prevent the spatial shaping of individual frequency components. The specified shaped pulses are generated with designed amplitude and phase masks.

Mode-locked laser produces a train of ultra-short pulses at a repetition rate, f_r, which is determined by the laser cavity length. The train of pulses generated by the laser can be expressed as

$$e(t) = u(t) \otimes \sum_{k=-\infty}^{\infty} \delta(t - kT), \qquad (1)$$

where $u(t)$ is the shape of the individual pulses, $T = 1/f_r$

is the repetition period, and $\otimes$ is the convolution operator.

In frequency domain, this can be expressed as follows:

$$E(f) = \frac{1}{T} \sum_{k=-\infty}^{\infty} U(kf_r) \delta(f - kf_r), \qquad (2)$$

where $U(f)$ is the Fourier transform of $u(t)$. The spectrum of the train of pulses has a comb-like structure, i.e., it consists of a large number of frequency components (laser modes) separated by the repetition rate of the laser[12,13].

The schematic of a pulse shaping apparatus is shown in Fig. 1. A liquid crystal (LC) spatial light modulator (SLM) has been used as a programmable mask to enable computer-controlled generation of waveforms.

It can be noted that the spatial mapping of the frequency components onto the mask is not linear and that this nonlinearity cannot be ignored for wide pulse bandwidths. The position of the center of the kth component on the mask is given by

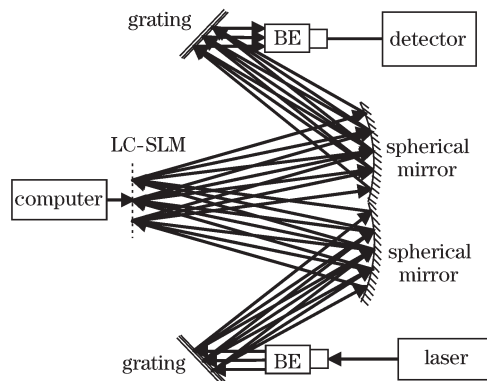$$x_k = F \tan(\theta_{dk} - \theta_d), \qquad (3)$$

Fig. 1. Schematic of the pulse shaping apparatus, BE: beam expander.

where F is the focal length of the lens, θ_{d} is the diffraction angle for the central component, and $\theta_{\mathrm{d}k}$ is the diffraction angle for the kth component. The diffraction angle is related to the wavelength through the grating equation for the first-order diffraction, as shown in the following equation:

$$\lambda_k = d(\sin\theta_{\mathrm{in}} + \sin\theta_{\mathrm{d}k}), \tag{4}$$

where λ is the wavelength of the kth spectral component, θ_{in} is the angle at which the input beam impinges on the diffraction grating, and d is the grating groove spacing. The spot size at the mask plane is also different with different spectral components:

$$a_k = \frac{4\lambda_k F \cos\theta_{\mathrm{in}}}{\pi a_{\mathrm{in}} \cos\theta_{\mathrm{d}k}}, \tag{5}$$

where a_k is the focal spot diameter of the kth comb line and a_{in} is the input beam diameter, both at e^{-1} level of the maximum field amplitude.

Ultra-short pulse laser emission is composed of immense number of frequency components. The focal spot formed by each component onto the mask has a finite size and, for a Gaussian beam, a Gaussian spatial intensity distribution. Individual focal spots usually overlap in space, indicating that different frequency components are not completely spatially separated (i.e., resolved). This is illustrated in Fig. 2, where the following parameters are used in the simulation: 60-fs pulses at 810 nm, laser repetition rate of 3 GHz, input beam diameter of 20 mm at e^{-1} level of the maximum field amplitude, input angle of 70°, grating groove spacing of 1/800 mm, and lens focal length of 30 cm.

The distance between two neighboring frequency components and the spot size of each frequency component at the mask plane are shown in Figs. 3(a) and (b), respectively.

In practice, the output waveform is shaped both in time and space due to the pixel nature of the mask and the finite spatial size of each frequency component. Wefers et al. have investigated theoretically and experimentally this space-time coupling phenomenon[4,7]. In most cases, the pulse shaping mask has a pixel structure and the light that impinges upon the pixel edges gives rise to diffraction effects because of the overlapping of focal spots of the individual frequency components (see Fig. 2). The diffraction of the pixel structure is manifested by
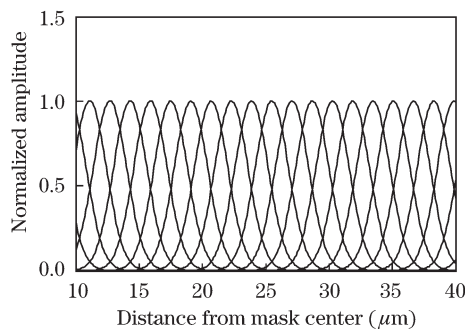
Fig. 2. Spatial intensity distribution on the mask plane of a pulse shaping system. The solid line indicates the focal spot intensity of individual spectral components.
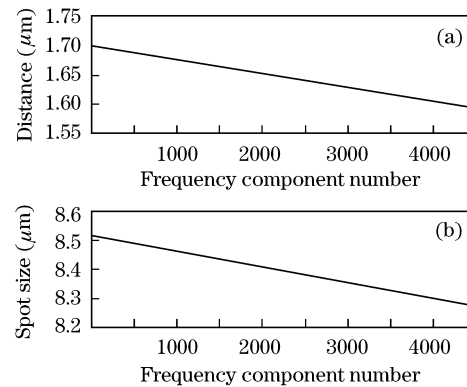
Fig. 3. (a) Distance between neighboring frequency components on the mask plane and (b) focused spot size of each frequency component on the mask plane.
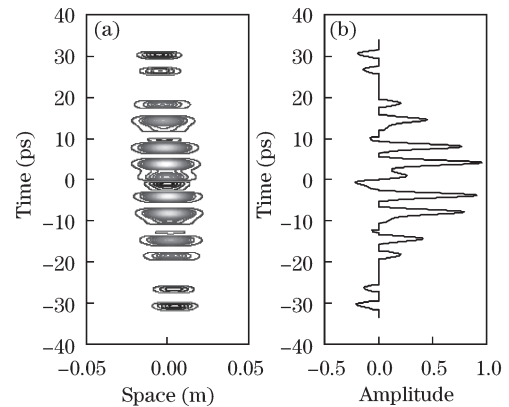
Fig. 4. Space-time profile of a waveform shape using the conventional pulse shaping technique. The intended waveform consists of four pulses of equal amplitude and phase. (a) Contour plot and (b) waveform amplitude profile at transverse position 0.

the appearance of high-order spatial modes in the output field. Another effect of the pixel structure of the mask is a sinc envelope function that modulates the output waveform[4,10]. Figure 4 shows the space-time profile of a shaped waveform when the individual frequency components are not spatially resolved. The parameters of the optical setup and the laser pulsed beam are the same as the ones used in Fig. 2, and the mask has a pixel structure with pixel size of 25 μm. The desired output waveform is a sequence of four identical pulses. Since the waveform occupies a significant part of the available temporal window (determined by the sinc envelope function), the replica pulses are clearly visible and cannot be neglected. Space-time coupling is manifested by a linear time-dependent spatial shift. The amplitudes of the side pulses are reduced due to the sinc envelope.

If each pixel of the pulse shaping mask filtered one and only one frequency component of the input pulse spectrum, and each component's focused spot fitted entirely and completely within the corresponding pixel, then the mask would effectively behave as a non-pixel structure mask. The shaped pulse would be free from all adverse effects arising from the finite spot size of the frequency components and the pixel structure of the mask. Here, we show how such operation of the pulse shaping appara-
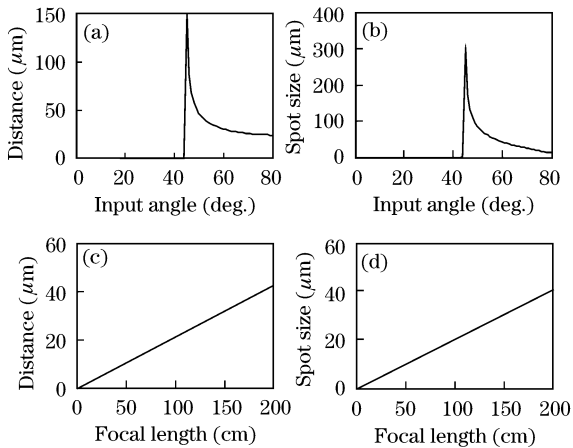
Fig. 5. (a) Distance between two neighboring frequency components changes with the input angle at focal length of 120 cm and (c) the focal length at incident angle of 70°; spot size of each frequency component changes with (b) the input angle at focal length of 120 cm and (d) the focal length at incident angle of 70°.
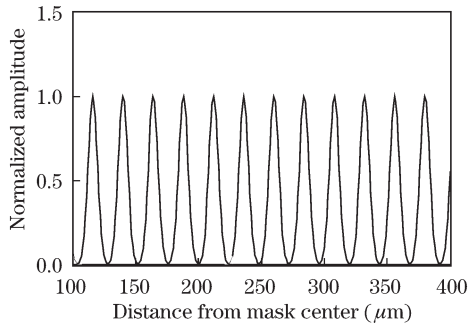

Fig. 6. Resolved pulse spectrum train based on the optimized pulse shaping system.

tus can be ensured. With the improved system, arbitrary waveforms can be generated with high accuracy.

The relationships of the distance and spot size with the parameters of the pulse shaping system at the central frequency component are shown in Fig. 5. As can be seen, we could choose an appropriate incident angle and a matched focal length to get the desired distance between two neighboring frequency components and the desired spot size of each frequency component on the mask plane.

Incident angle of 70°, input beam diameter of 40 mm, grating groove space of 1/2100 mm, and focal length of the mirror of 120 cm were used as the parameters of our pulse shaping system for the simulation. The resolved pulse train based on this pulse shaping system is shown in Fig. 6. The corresponding distance between two neighboring frequency components and the spot size of each frequency component are shown in Figs. 7(a) and (b), respectively.

Ideally, upon exiting the pulse shaping apparatus with optimized parameters, the shaped pulse should have the desired temporal waveform and unchanged spatial intensity distribution.

When the fine structure of the comb-like spectrum is resolved, the mask can be designed as a pixel structure with each pixel filtering only one frequency component.

This solves the space-time coupling problem. Additionally, the edges of the mask pixels are not illuminated because no frequency component bridges the two neighboring pixels. As such, there is no diffraction off the pixel mask structure and higher-order spatial modes are not present in the output waveform.

On the masking plane, the mask filters the spectral content of the input pulse train linearly. The actual output pulse train can then be expressed in the frequency domain as follows:

$$E_{\text{out}}(f) = \frac{1}{T} \sum_{k=-\infty}^{\infty} U(kf_{\text{r}}) M(kf_{\text{r}}) \delta(f - kf_{\text{r}}), \quad (6)$$

where $M(kf_{\text{r}})$ is the complex transmission of the mask for the kth frequency component.

On the other hand, the target output from the pulse shaping system is again a train of pulses and can be expressed in time and frequency domains similar to Eqs. (1) and (2):

$$e_{\text{out}}^{\text{target}}(t) = r(t) \otimes \sum_{k=-\infty}^{\infty} \delta(t - kT), \quad (7)$$

$$E_{\text{out}}^{\text{target}}(f) = \frac{1}{T} \sum_{k=-\infty}^{\infty} R(kf_{\text{r}}) \delta(f - kf_{\text{r}}), \quad (8)$$
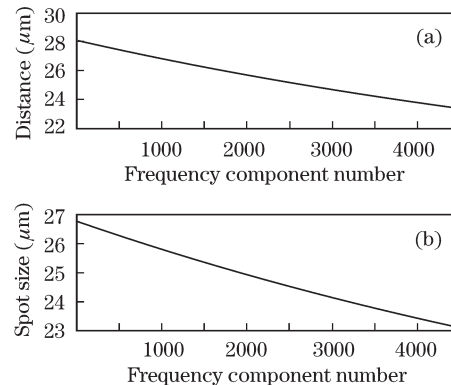

Fig. 7. (a) Distance between two neighboring frequency components and (b) spot size of each frequency component based on the optimized pulse shaping system.
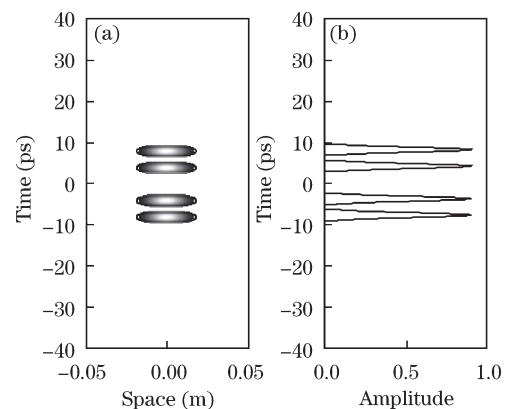

Fig. 8. Space-time profile of the waveform from Fig. 4 that was shaped using the proposed novel pulse shaping technique. (a) Contour plot and (b) waveform amplitude profile at transverse position 0.
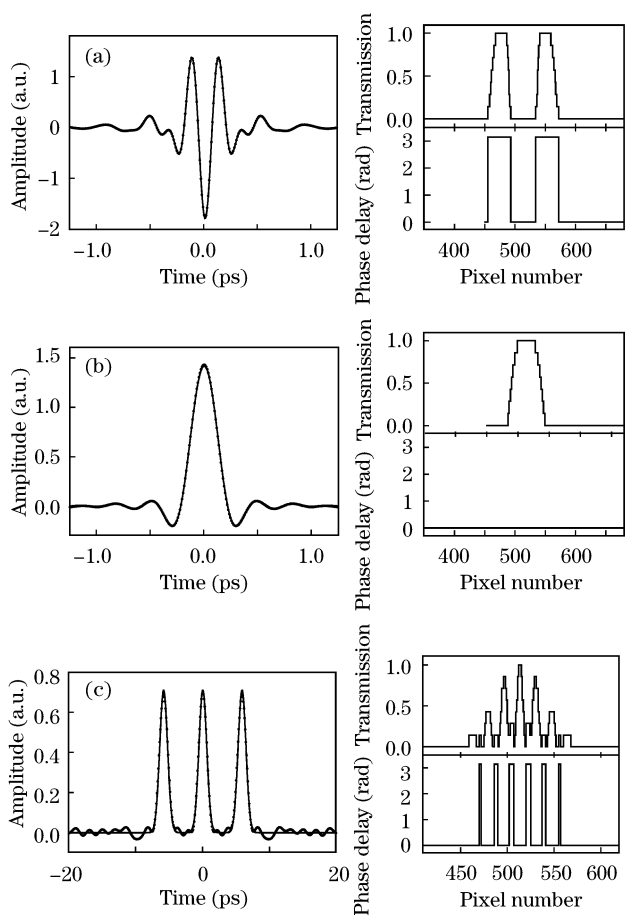
Fig. 9. Left column: simulated shaped pulses (dots) and the corresponding target waveforms (solid line); right column: amplitude and phase mask patterns. (a) Meyer wavelet of order 4; (b) square root raised cosine; and (c) sequence of three identical pulses.

where $r(t)$ is the desired output pulse shape and $R(f)$ is its Fourier transformation.

By comparing Eqs. (6) and (8), the desired complex transmission of the mask is computed through

$$M(kf_{\mathrm{r}}) = \frac{R(kf_{\mathrm{r}})}{U(kf_{\mathrm{r}})}. \qquad (9)$$

Neither space-time coupling nor higher-order spatial modes are present in the output pulse, as evident from Fig. 8, where the space-time profile of the shaped pulse is shown for the case of Fig. 4.

In practice, the output waveform differs from the desired one. The actual mask transmission is obtained from Eq. (6) after quantizing the mask transmission values according to the available number of gray levels. Assuming a Gaussian input electric field, we have designed eight-level amplitude and phase masks that generate different waveforms. Figure 9 shows the simulated output waveforms in comparison to the targeted waveforms.

The examples include a Meyer wavelet (Fig. 9(a)) and a square root raised cosine pulse (Fig. 9(b)), which are of particular importance to communications[1,2], as well as a sequence of three identical pulses that are 6 ps apart (Fig. 9(c)). The quantization error in the last example results in ripples between the pulses and causes a slight reduction in the amplitude of the two outer pulses. The significant quantization error is due to the extremely fine features in the targeted spectrum, which could not be reproduced exactly by the eight-level masks.

In conclusion, we have devised an improved pulse shaping system, which we can use to simulate truly arbitrary waveform. Using an optimized high-resolution pulse shaping apparatus, we have shown that it is possible to resolve the spectral components that make up the pulse train, allowing for the independent filtering of each individual frequency component. The resultant shaped waveforms are free from space-time coupling effects and high-order spatial modes. Meyer wavelet and square root raised cosine waveforms are simulated and compared with the target pulses. These waveforms have been successfully obtained using masks with an eight-level pixel structure, which can potentially improve the availability and throughput of optical wireless communication systems.

References

1. M. Kavehrad and B. Hamzeh, Proc. SPIE **5598,** 144 (2004).
2. M. Kavehrad and B. Hamzeh, in *Proceedings of IEEE MILCOM* 398 (2004).
3. F. Courvoisier, V. Boutou, J. Kasparian, E. Salmon, G. Méjean, J. Yu, and J. P. Wolf, Appl. Phys. Lett. **83,** 213 (2003).
4. M. M. Wefers and K. A. Nelson, J. Opt. Soc. Am. B **12,** 1343 (1995).
5. A. Efimov, C. Schaffer, and D. H. Reitze, J. Opt. Soc. Am. B **12,** 1968 (1995).
6. A. M. Weiner, Prog. Quantum Electron. **19,** 161 (1995).
7. M. M. Wefers and K. A. Nelson, IEEE J. Quantum Electron. **32,** 161 (1996).
8. K. Takasago, M. Takekawa, M. Suzuki, K. Komori, and F. Kannari, IEEE J. Sel. Top. Quantum Electron. **4,** 346 (1998).
9. A. M. Weiner and A. M. Kan'an, IEEE J. Sel. Top. Quantum Electron **4,** 317 (1998).
10. D. H. Reitze, A. M. Weiner, and D. E. Leaird, Appl. Phys. Lett. **61,** 1260 (1992).
11. R. Holzwarth, M. Zimmermann, T. Udem, and T. W. Hänsch, IEEE J. Quantum Electron. **37,** 1493 (2001).
12. J. Rauschenberger, T. M. Fortier, D. J. Jones, J. Ye, and S. T. Cundiff, Opt. Express **10,** 1404 (2002).
13. G. Minguez-Vega, J. D. McKinney, and A. M. Weiner, Opt. Express **13,** 8056 (2005).
14. C. B. Huang, Z. Jiang, D. E. Leaird, and A. M. Weiner, Electron. Lett. **42,** 1114 (2006).
15. Z. Jiang, D. E. Leaird, and A. M. Weiner, J. Lightwave Technol. **24,** 2487 (2006).
16. W. Wang, R. Zhao, J. Su, H. Li, Y. Liang, L. Mo, F. Wang, L. Liu, Z. Sun, Q. Zhu, and F. Jing, Acta Opt. Sin. (in Chinese) **30,** 1051 (2010).
17. Y. Zhao, X. Zheng, H. Zhang, and B. Zhou, Chin. Opt. Lett. **8,** 454 (2010).